

This is an Open Access document downloaded from ORCA, Cardiff University's institutional repository: <https://orca.cardiff.ac.uk/id/eprint/158336/>

This is the author's version of a work that was submitted to / accepted for publication.

Citation for final published version:

Al Zoubi, Wail, Assfour, Bassem, Wahab Allaf, Abdul, Leoni, Stefano , Kang, Jee-Hyun and Ko, Young Gun 2023. Experimental and theoretical investigation of high-entropy-alloy/support as a catalyst for reduction reactions. *Journal of Energy Chemistry* 81 , pp. 132-142. 10.1016/j.jechem.2023.02.042

Publishers page: <http://dx.doi.org/10.1016/j.jechem.2023.02.042>

Please note:

Changes made as a result of publishing processes such as copy-editing, formatting and page numbers may not be reflected in this version. For the definitive version of this publication, please refer to the published source. You are advised to consult the publisher's version if you wish to cite this paper.

This version is being made available in accordance with publisher policies. See <http://orca.cf.ac.uk/policies.html> for usage policies. Copyright and moral rights for publications made available in ORCA are retained by the copyright holders.



Experimental and theoretical investigation of high-entropy-alloy/support as a catalyst for reduction reactions

Wail Al Zoubi ^{a,†}, Bassem Assfour ^b, Abdul Wahab Allaf ^{b,c}, Stefano Leoni ^d, Jee-Hyun Kang ^e, Young Gun Ko ^{a,†}

^a Materials Electrochemistry Laboratory, School of Materials Science and Engineering, Yeungnam University, Gyeongsan 38541, Republic of Korea

^b Atomic Energy Commission, Department of Chemistry, P.O. Box 6091, Damascus, Syria

^c Arab International University, Department of Pharmaceutical Chemistry and Quality Control, Faculty of Pharmacy, Ghabaghib, Darra, Syria

^d Cardiff University, School of Chemistry, Park Place, CF10 3AT Cardiff, United Kingdom

^e School of Materials Science and Engineering, Institute of Materials Technology, Yeungnam University, Gyeongsan 38541, Republic of Korea

article info

Keywords:

Plasma
Miscible
Multicomponent
Metal nanoparticle
Nanocatalysts

abstract

Control of chemical composition and incorporation of multiple metallic elements into a single metal nanoparticle (NP) in an alloyed or a phase-segregated state hold potential scientific merit; however, developing libraries of such structures using effective strategies is challenging owing to the thermodynamic immiscibility of repelling constituent metallic elements. Herein, we present a one-pot interfacial plasma-discharge-driven (IP-D) synthesis strategy for fabricating stable high-entropy-alloy (HEA) NPs exhibiting ultrasmall size on a porous support surface. Accordingly, an electric field was applied for 120 s to enhance the incorporation of multiple metallic elements (i.e., CuAgFe, CuAgNi, and CuAgNiFe) into alloy HEA-NPs. Further, NPs were attached to a porous magnesium oxide surface via rapid cooling. With solar light as the sole energy input, the CuAgNiFe catalyst was investigated as a reusable and sustainable material exhibiting excellent catalytic performance (100% conversion and 99% selectivity within 1 min for a hydrogenation reaction) and consistent activity even after 20 cycles for a reduction reaction, considerably outperforming the majority of the conventional photocatalysts. Thus, the proposed strategy establishes a novel method for designing and synthesizing highly efficient and stable catalysts for the conversion of nitroarenes to anilines via chemical reduction.

1. Introduction

Combination and interconnection of interdisciplinary areas, technologies, and sciences have led to rapid advances in a vast range of areas. In nanotechnology and nanoscience, the combination of multicomponent nanoparticles (NPs) and interdisciplinary research is particularly important because a majority of significant discoveries in previous fields occur at the intersection of multiple nanoscale domains in terms of their applications and conceptualization [1,2]. Unlike monometallic materials, in the field of NPs, multimetallic alloy catalysts exhibit excellent physical and chemical properties, either by (i) facilitating hybrid magnetic, electronic, and chemical interactions between metal precursors [2] or (ii) merging dissimilar properties associated with each component, with an expansive and underexplored compositional space,

because of the presence of various elements in a single NP and the association of strong synergistic effects of physicochemical properties of individual components [3]. Among various alloy materials, high-entropy-alloy nanoparticles (HEA-NPs) (i.e., single-phase or equimolar) pose formidable challenges that cannot be using corresponding monometallic counterparts [4,5]. HEA-NPs have been used in tunable catalysis, chemical sensors, and drug delivery as well as possess high chemical/thermal stabilities against corrosion and oxidation [4].

Synthesizing HEA-NPs requires precise control of reaction conditions, which has been difficult to achieve using site-specific synthesis techniques, including traditional wet-chemistry synthesis [6], two-step carbothermal shock (CTS) method [7], and lithography-based synthesis [8], owing to the slow rates of cooling/heating process that facilitate the agglomeration and growth of NPs and limit the compositional space/structural complexity to phase-separated HEA-NPs, particularly for immiscible elemental combinations [9]. Formation of multiple elements is primarily driven by a high temperature (2000 K) among metallic species to

[†] Corresponding authors.

E-mail addresses: wailalzoubi@ynu.ac.kr (W. Al Zoubi), younggun@ynu.ac.kr (Y.G. Ko).

build high-entropy structures ($\Delta G = \Delta H - T \Delta S$), which explains why the majority of published alloy NPs prepared using wet-chemistry approaches does not include three metals [10]. For instance, Yao et al. have reported high-throughput synthesis of multimetallic nanoclusters loaded on surface-treated carbon supports as promising catalytic materials using two steps: (i) combinatorial chemical composition design by mixing in the solution phases and (ii) a rapid thermal-shock treatment (i.e., 1700 K, 500 ms) of salt precursor-loaded carbon support to decompose metal salts [7]. Additionally, an HEA-Pt₁₈Ni₂₆Fe₁₅Co₁₄Cu₂₇ catalyst was fabricated using a low-temperature one-pot oil phase synthesis approach at 222 °C for 120 min for methanol oxidation reactions and hydrogen evolution reactions (HERs) [9]. Moreover, alloying of immiscible metal elements into single NPs (average size of NP 5 nm) loaded onto carbon support (e.g., carbon nanofibers) utilizes a two-step CTS process based on flash heating (temperature = 2000–3000 K, shock duration = 55 ms, and rate 10^5

s⁻¹) and quick quenching [10]. Qiao et al. [11] utilized this quick, high-temperature heating process to prepare HEA-NPs on a carbon-based substrate, which has an average particle size of 12 nm owing to the breakdown of precursors into liquid metal solidification. Carbon-based materials, such as carbon nanofibers and carbonized wood, can be employed as substrates at temperatures exceeding 1400 K. At 923 K, Gao et al. demonstrated a pyrolysis strategy following wet impregnation to immobilize HEA-NPs dispersed on granular supports such as alumina oxides, active carbon, and zeolite (Permutit) [12]. Based on the above, the aforementioned methods for fabricating of NPs have limitations. Consequently, it is difficult to develop an effective technique for preparing supported HEA-NPs catalysts exhibiting high stability in one-step because dispersed NPs on a support require an additional carbonization step to achieve high conductive material. Further, downsizing HEA-NPs to tens of nanometers is a formidable task, particularly using traditional alloying techniques [13–23]. Accordingly, the development of a one-step chemical oxidation and reduction method for preparing stable supported HEA-NP catalysts that yield a new array of nanostructures and alloys exhibiting excellent capabilities and cycling performance is challenging. Herein, we proposed a facile and ultrafast (2 ms), one-pot interfacial plasma-discharge-driven (IP-D) synthesis strategy

using soft plasma discharges (a voltage of < 300 V, a temperature of 2000 K, and an ultrafast plasma discharge duration of 10 ms) to decompose additional salt precursors to metallic NPs and oxidize the metal plate as a coating layer, at metal-alkaline electrolyte [comprising a green reductant (ethylene glycol) and phosphate] interfaces. This simultaneously yields HEA-NPs (i.e., CuAgFe, CuAgNi, and CuAgNiFe) of dissimilar metallic elements on a defective oxide layer (Table S1). The multielement (ME) NPs and porous material support synthesized using IP-D process have an HEA and a limited size distribution despite being subjected to high temperatures that often promote particle coarsening. Additionally, in conjunction with the reduction activities of ethylene glycol and the oxidation of the Mg metal plate, the soft plasma discharges cause the rapid “fusion” of particles, yielding homogeneous chemical mixtures of multiple elements. Consequently, high-voltage discharge during IP-D forms HEA-NPs and facilitates the anchoring and stability of the NPs in porous structures once they have been prepared, owing to their extremely strong interaction with the support. By adjusting the applied voltage, plasma effect, and concentration of utilized reducing agents, we can also manufacture uniform HEA-NPs by reducing the reaction time. The IP-D method can be used for generating of alloys and HEA-NPs, exhibiting redox potentials for a wide variety of applications. With solar light as the energy input, CuAgFeNi catalyst supported on P-MgO operates through the adsorption and interaction between hydrazine and the catalyst to improve the cat-

alytic reduction of 4-nitrophenol, as clarified by density functional theory (DFT). We believe that the mechanistic explanation documented herein will guide the preparation of HEA-NPs exhibiting ultrasmall sizes via soft plasma discharge-based methods as well as pave the way for the discovery of practical application of HEA-NPs and other excellent rapid high-temperature synthesis strategies.

2. Experimental

2.1. Materials

Silver nitrate (AgNO₃), Copper (II) nitrate (Cu(NO₃)₂ · 3H₂O), nickel(II) nitrate hexahydrate (Ni(NO₃)₂ · 6H₂O), iron(III) nitrate nanohydrate (Fe(NO₃)₃ · 9H₂O), hydrazine (H₂NNH₂), ethylene glycol (C₂H₆O₂), and all the nitroarene compounds were purchased from Merck, and used as received. Magnesium alloys of 10 mm-thick into 10 × 20 × 4 mm plates using wire electrical discharge machining.

2.2. IP-D method: Experimental procedure

A MgO support was deposited on Mg alloy by applying a 60 Hz frequency for 120 s to an anode immersed in an electrolyte of 6 g L⁻¹ KOH, 30 g L⁻¹ C₂H₆O₂, 8 g L⁻¹ K₃PO₄ in 2 L of DI water (pH = 13). IP-D is a conventional anodic oxidation method used to prepare a porous inorganic layer on the MgO substrate. Metal ions were reduced to Cu, Ag, Ni, and Fe, respectively, with the addition of AgNO₃, Cu(NO₃)₂ · 3H₂O, Ni(NO₃)₂ · 6H₂O, and Fe(NO₃)₃ · 9H₂O to a phosphate-based electrolyte containing C₂H₆O₂ as the reducer. MgO-supported Mg alloy was subjected to spontaneous oxidation–reduction–precipitation reactions at 0 LC, 60 Hz, and 120 s in a phosphate-based electrolyte.

The MgO support grew gradually in thickness due to an applied voltage.

IP-D demonstrates many electrochemical processes. (I) Evolution of oxygen at the common anode, (II) oxidation of Mg alloy, and (III) reduction of metal salts in the electrolyte. Depending on the composition and chemical activity of the electrolyte, oxidation may cause either surface dissolution or the formation of a MgO support. The reactions occurred as shown in the following equations.



During the IP-D process, the growth of HEA-NPs and MgO support increased in the voltage. Meanwhile, micro-arc-discharge (MAD) triggered the breakdown-voltage and accelerated the formation of the porous MgO layer. MAD increases the local electron temperature, initiating a plasma discharge chemical reaction at the arcing sites. During these plasma-chemical reactions, the Mg surface was gasified and oxidized to produce defective MgO support, and the metal ions [i.e., Cu(NO₃)₂, AgNO₃, Fe(NO₃)₂, and Ni(NO₃)₂] in the electrolyte solution, which forwarded to the Mg anode, were reduced at a high local temperature in the discharge channel in the presence of ethylene glycol to produce CuAgFeNi NPs. CuAgFeNi NPs were quenched simultaneously by the plasma discharge, forming CuAgFeNi-P-MgO catalysts on the Mg plate

surface. Consequently, a unique embedded structure was produced, promoting the firm anchoring of CuAgFeNi NPs to the porous MgO support surface.

Gradually, the arc discharge intensified and the thickness of the defective MgO coating containing CuAgFeNi NPs increased quickly, increasing the voltage. Once the thickness of the support reached a predetermined threshold, the film could no longer be broken down at high voltages owing to its high resistance. Consequently, the arc discharge disappeared gradually, indicating the end of the IP-D process.

2.3. Characterization

More details are provided in [supplementary materials](#).

2.4. Catalytic reduction of nitroarene compounds

On the Mg alloy surface, 5–15 mg of CuAgFeNi/P-MgO catalyst was precipitated on the Mg by adding 4 ppm of 4-nitrophenol, 5 mL of hydrazine hydrate (50% solution), 4 mL of ethanol, and 3 mL methylamine. After stirring, a 100-mL round-bottom flask was irradiated in a photoreactor equipped with a light source (a 10-W UV lamp, $\lambda = 254$ nm was employed as the light source) for 0 to 3 h at 25 °C. For further analyses, the chloroform solution of the product was diluted and analyzed using HPLC (see the [supplementary materials](#)). Products were identified by comparing the retention duration to that of standard chemicals, and the quantitative composition of each component was analyzed using HPLC by interpolating the calibration curves.

Below are the equations (6–8) used to calculate the conversion and selectivity.

$$\text{Conversion } \delta\% = \frac{\text{Moles all products}}{\text{Moles of reactant}} \times 100 \quad (6)$$

$$\text{Selectivity } \delta\% = \frac{\text{Moles of desired product}}{\text{Moles of all products}} \times 100 \quad (7)$$

$$\text{TOF } \frac{1}{\text{h}} = \frac{\text{Moles of desired product}}{\text{Moles of catalyst} \times \text{hours of reaction}} \quad (8)$$

Herein, we calculate the turnover frequency (TOF) using the CuAgFeNi/P-MgO catalyst because the support is an integral part of catalytic activity.

2.5. Computational details

Using DFT, the structural and electronic properties of the synthesized nanoparticles were analyzed. As the initial structure, we used a cubic structure of Ag containing eight atoms of Ag mounted on a MgO substrate (5 × 5 × 3-unit cells). After optimizing the structure, the bandgap and density of states (DOSs) were calculated. The value of the lattice constant corresponded well with the reported data. These calculations were performed using the hybrid Perdew–Burke–Ernserhof (PBE) GGA functional. The D3-grimme dispersive corrections, and plane-wave cutoff energy was calculated 70 Ry (952 eV). The external electric field used to compute the electrical characteristics ranges from 0.1 V/Å to 0.6 V/Å. All the calculations were performed using the computer program Quantum ESPRESSO.

To explore and investigate the mechanism of hydrazine dissociation, molecular dynamics (MD) simulations were performed. Except for the additional hydrazine molecule, the simulation system is the same as it was previously in [Fig. 1](#). All the atoms were free to move during MD simulations. The atomic coordinates and energies of trajectory were recorded for 5 ps with a time step of 0.5 fs.

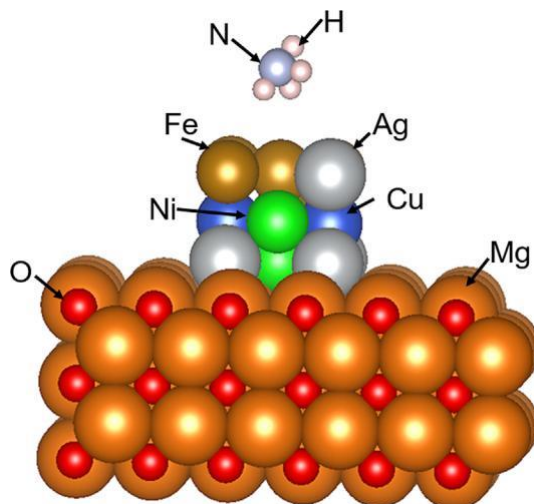


Fig. 1. Simulation system is the same as before in addition to on hydrazine molecule.

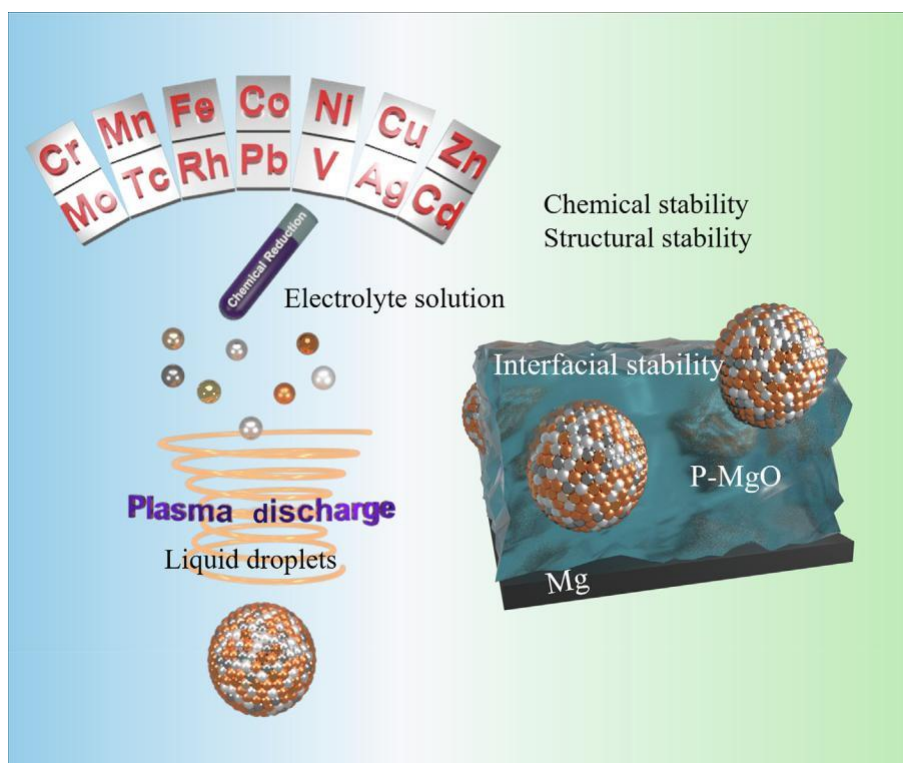
2.6. Thermodynamic calculations

Ternary phase diagrams, mixing enthalpy (ΔH_{mix}), and entropy (ΔS_{mix}) were calculated using ThermoCalc 2022 with SSOL data-base. The mixing Gibbs free energy was then estimated using the formula, $\Delta G_{\text{mix}} = \Delta H_{\text{mix}} - T\Delta S_{\text{mix}}$ at various temperatures. For calculating ΔH_{mix} and ΔS_{mix} , the compositions of the NPs obtained using EDS ([Fig. S1](#)) were used as input. The liquid was chosen as the coexisting phase because multielement solutions at high local temperatures would exist as liquid droplets.

3. Results

3.1. Synthesis of HEA-NPs

Conventionally, vapor-phase dispositions and thermal-shock treatments can generate a large number of NPs using a chemical composition gradient [7]; however, they require multiple element steps, complex and expensive equipment, and a limited selection of elements and supports. Conversely, a series of HEA-NPs, from ternary (CuAgFe and CuAgNi) to quaternary (CuAgFeNi) HEA-NPs, were synthesized using a straightforward one-pot strategy, with water as the solvent by adding a mixture of salt precursors M_xCl_y ($M = \text{Ag, Cu, Fe, and Ni}$) through plasma-assisted electrochemical reactions at 0 °C for 3 min. Driven by high electrical field plasma (10^6 V/cm) at the local plasma temperature (>2000 K) in a discharge channel as well as the oxidation of the Mg metal plate, which occurs when molten Mg flows out of the channel, the high temperature and reducing agents (1,2,3-propanetriol and 1,2-diethanediol) induce rapid thermal decomposition (reduction) of the hydrolyzed precursors to form metal atoms that are mixed with each other, generating small liquid droplets of multimetallic solutions that rapidly cool at the surface–support interfaces ([Scheme 1](#)) [21]. However, because of the very small and brief localized plasma discharges, metallic atoms cannot spread over a considerable distance to facilitate the agglomeration of HEA-NPs on the porous magnesium oxide (P-MgO) surface. Instead, metallic atoms are kinetically entrapped by porous surfaces, forming HEA-NPs ([Figs. S1 and S2](#)). Upon rapid cooling of the electrolytic solution, these nonvolatile liquid droplets crystallized into homogeneous and alloy HEA-NPs without agglomeration/aggregation, phase separation, or element segregation. Additionally, the size



Scheme 1. Schematic of the CuAgFeNi/P-MgO fabrication process using IP-D synthesis strategy and reduction of nitro-aromatic compounds.

of HEA-NPs can be tuned by varying the duration of the plasma and dropwise: a shorter IP-D yields NPs (Fig. S3).

Using inductively coupled plasma atomic emission spectroscopy (ICP-AES), the metal compositions of HEA-NPs were determined to be 12:73:15, 9:82:7, and 17:54:14:15 for CuAgFe HEA-NPs, CuAgNi HEA-NPs, and CuAgFeNi HEA-NPs, respectively. High-resolution transmission electron microscopy (HR-TEM) images of CuAgFeNi HEA-NPs show that the morphology of the surface and cross-section is fused to the P-MgO surface (denoted

as CuAgFeNi/P-MgO), and the diameter is 1.6 ± 0.5 nm (Fig. S4). Additionally, the HR-TEM (Fig. 2) image for CuAgFeNi HEA-NPs and Fig. S5 for CuAgFe HEA-NPs and CuAgNi HEA-NPs reveal that the lattice spacing is 0.14 and 0.21 nm corresponding to the (111) plane. As shown in Fig. 2(a-d), the HR-TEM results of the distribution of CuAgFeNi HEA-NPs are distributed with a diameter of <2 nm in the outer layer, while the diameter is > 2 nm in the inner layer because the diffusivity of atoms or ions depends on plasma temperature and the thickness of P-MgO, which reduces the aggregation and sintering of the HEA-NPs. This can be explained by the fact that the number and density of the sparks decreased between 100 and 120 s owing to a thicker support layer, making the initiation of such discharges more difficult (real-time images, Fig. S6), limiting particle growth and preventing agglomeration in the top-layer. On the P-MgO support, the formed CuAgFeNi HEA-NPs are uniformly distributed and crystallized (Fig. 2e-h). X-ray diffraction (Fig. S7) also confirms the close interfacial interaction between the NPs and P-MgO support. Accordingly, four metal elements comprise HEA in a single FCC structure with a lattice constant 2.1 Å. Moreover, the distance of 0.14 and 21 nm between adjacent lattice fringes of CuAgFeNi NPs can be indexed to the d spacing of the (111) plane of FCC. Additionally, Fig. 2(i-m) illustrates energy-dispersive X-ray spectroscopy (EDX) measurements, revealing that Cu, Ag, Fe, and Ni elements coexist in single NPs and are almost uniformly distributed throughout the NPs, elucidating the effective preparation of HEA-NPs (Figs. S8 and S9). Further

analysis shows that Cu, Ni, and Fe are more concentrated in the center of the NP, with a shell comprising Ag elements. This is likely because Ag/Ag^+ ($E^0 = 0.8$ V) exhibiting a high positive reduction potential can displace the metal elements with a lower reduction potential, i.e., Cu/Cu^{2+} ($E^0 = 0.34$), Ni/Ni^{2+} ($E^0 = 0.25$ V), and Fe/Fe^{3+} ($E^0 = 0.04$ V), from the edge of the NP, and therefore, they are more prone to oxidation than Ag owing to their low reduction potentials [25].

Further analysis of HEA-NPs using high-angle annular dark-field scanning transmission electron microscopy (HAADF-STEM) (Fig. 3a-f and Fig. S10) revealed the unexpected presence of small CuAgFe, CuAgNi, and CuAgFeNi HEA-NPs with mean diameters of 5, 3.7, and 3.8 nm, respectively. Additionally, they were uniformly distributed over the defect structure and a certain amount of single atoms was dispersed on the P-MgO support. These results revealed that heat treatment at a local plasma electron temperature with a short lifetime of 2000–3000 K through an electrical field did not induce considerable agglomeration and sintering, demonstrating the advantage of the defects and plasma discharge, including melting, melt-flow, and resolidification, as nucleation sites for housing Ag, Cu, Fe, and Ni particles and particle dispersion in the outer layer (Fig. S8). Moreover, the rapid melting-cooling process of NPs within the discharge channel occurs so quickly that HEA-NPs in the melted site do not have time to agglomerate or even nucleate. To analyze the chemical states and binding nature of the elements present in CuAgFeNi HEA-NPs, an X-ray photoelectron spectrum of the surface region (1 nm in depth, as determined by the beam energy of Al K α) was obtained (Fig. 3). The main peaks at 1303.14 and 1303.73 eV in the high-resolution Mg 2p XPS profile of CuAgFeNi/P-MgO were assigned to P-MgO and $\text{Mg}_3(\text{PO}_4)_2$, respectively, confirming the presence of Mg in the as-prepared support [26]. Additionally, the results of XPS indicate that all the elements in HEA-NPs are in metallic states. Fig. 3(h–l) shows the descriptive XPS spectra for Ag, Cu, Fe, and Ni elemental compositions. Accordingly, the two peaks associated with the Ag 3d $_{5/2}$

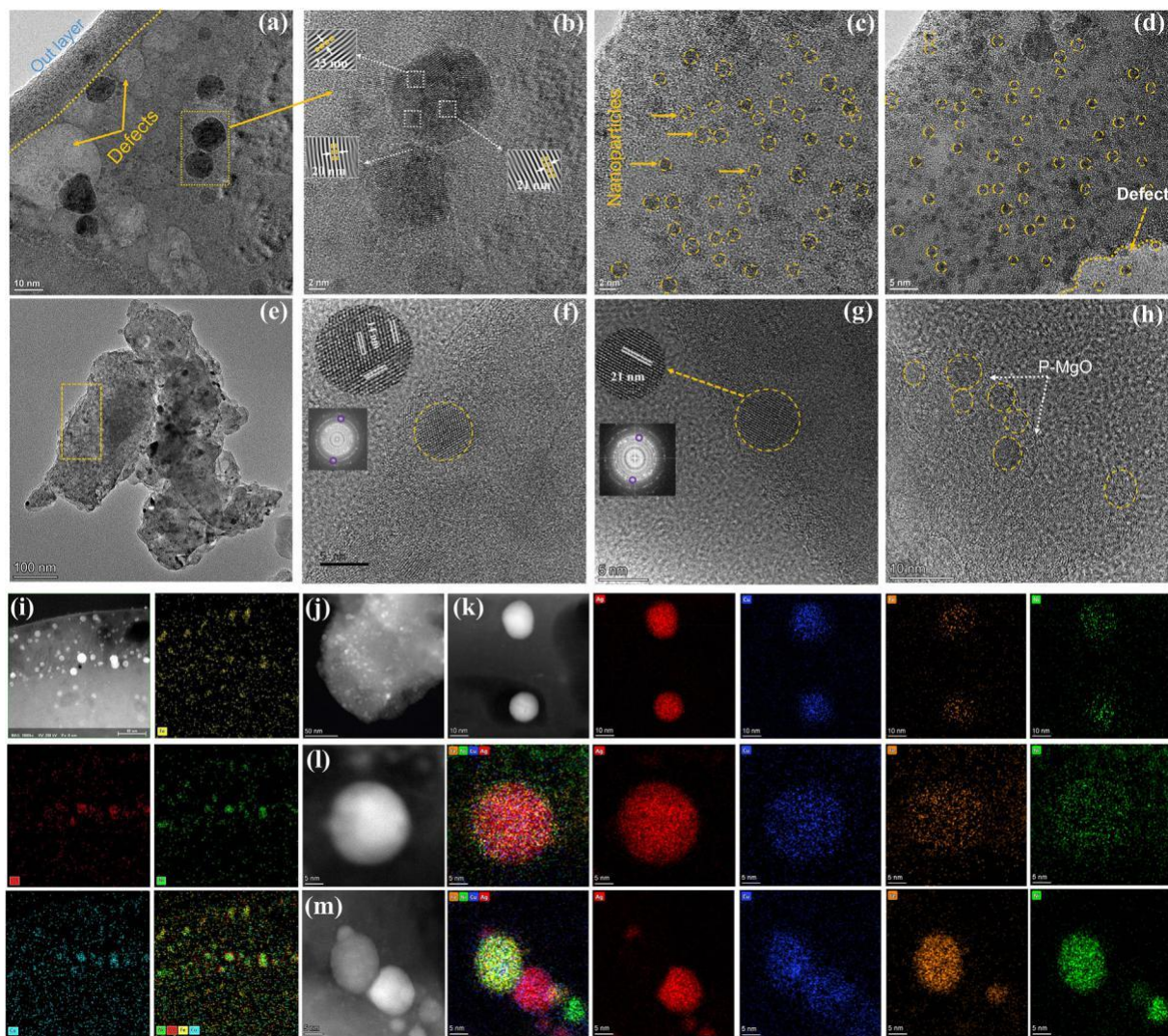


Fig. 2. HR-TEM and elemental mapping analysis. (a) TEM image of the cross-sections of CuAgFeNi HEA-NPs encapsulated by the P-MgO support, (b) HR-TEM image of the CuAgFeNi HEA-NPs in the inner layer of support, (c and d) HR-TEM image of the CuAgFeNi HEA-NPs on the outer layer of the support surface, (e–h) HR-TEM images of the CuAgFeNi HEA-NPs and the P-MgO support on the surface, and (i–m) HAADF-STEM images and EDX chemical mappings of Ag, Cu, Fe, and Ni in the CuAgFeNi HEA-NPs.

and 3d_{3/2} doublet were detected at 366.80 and 372.85 eV, indicating the metallic state of Ag in HEA-NPs, whereas the shake-up peaks disappeared and Cu 2p_{3/2} and 2p_{1/2} peaks appeared at Cu⁰ (932.02 eV) and Cu²⁺ (952.01 eV), respectively, indicating the presence of metallic copper [24–26]. Correspondingly, charge transfer between the metals in CuAgFeNi HEA-NPs may not be considerable. Moreover, the Ni 2p spectra reveal the presence of Ni⁰ (854.8 and 872.36 eV) and Ni²⁺ (860.44 and 878.56 eV), confirming the presence of Ni²⁺ owing to the high chemical activity of Ni. Furthermore, the Fe 2p spectra display two peaks at 710.28 and 723.30 eV corresponding to Fe 2p_{3/2} and Fe 2p_{1/2}, respectively [27].

3.2. Reduction-reaction performance of CuAgFeNi HEA-NPs

The reduction activity of CuAgFeNi HEA-NPs for the hydrogenation of nitroarenes (Fig. 4a) was assessed using 2-propanol (secondary alcohol) and hydrazine as the electron donor and hydrogen source, respectively. Hydrazine and 2-propanol are advantageous because of the hydrogen-donor ability and easily separable thermodynamically stable products (only hydrogen and nitrogen are generated by hydrazine and acetone is generated by 2-propanol, which can act as the hydrogen acceptor) [28,29]. Cor-

respondingly, excess 2-propanol is required during the reduction reaction, and the presence of hydrazine and P-MgO as bases helps extract dihydrogen from alcohol. Reduction-reaction optimization using 8 mg of the CuAgFeNi HEA-NP catalyst deposited on the magnesium surface revealed that 4-aminophenol (4AP) was produced within 2 h in the presence of 10-mM hydrazine with 85% conversion and 80% selectivity using 1.35 mM of 4NP (Fig. 4b, left section) under 450-nm light. By increasing the concentration of 4NP to 2.5 mM in the presence of 10-mL 2-propanol, 100% conversion and selectivity were attained after 3 h of reduction reactions (Fig. 4b, middle section), corresponding to a TOF of 13.5 h⁻¹, which is among the highest reported values (Table S2). The efficiency of NPs catalysts was determined by increasing the 4NP concentration to 4 mM under the same experimental conditions, generating 4AP in 100% yield and selectivity, corresponding to the highest TOF value of 20 h⁻¹ compared to other publications (Fig. 4b, right section). In the absence of the catalyst and hydrogen donor, the reduction reaction did not yield any 4AP under light or darkness, indicating the high catalytic activity of CuAgFeNi HEA-NPs (Fig. 4c).

To gain further insights, we found that the conversion and rate of the reduction reaction depended on the amount of catalyst (Fig. 4c), with the highest conversion and TOF value of 20 h⁻¹ with

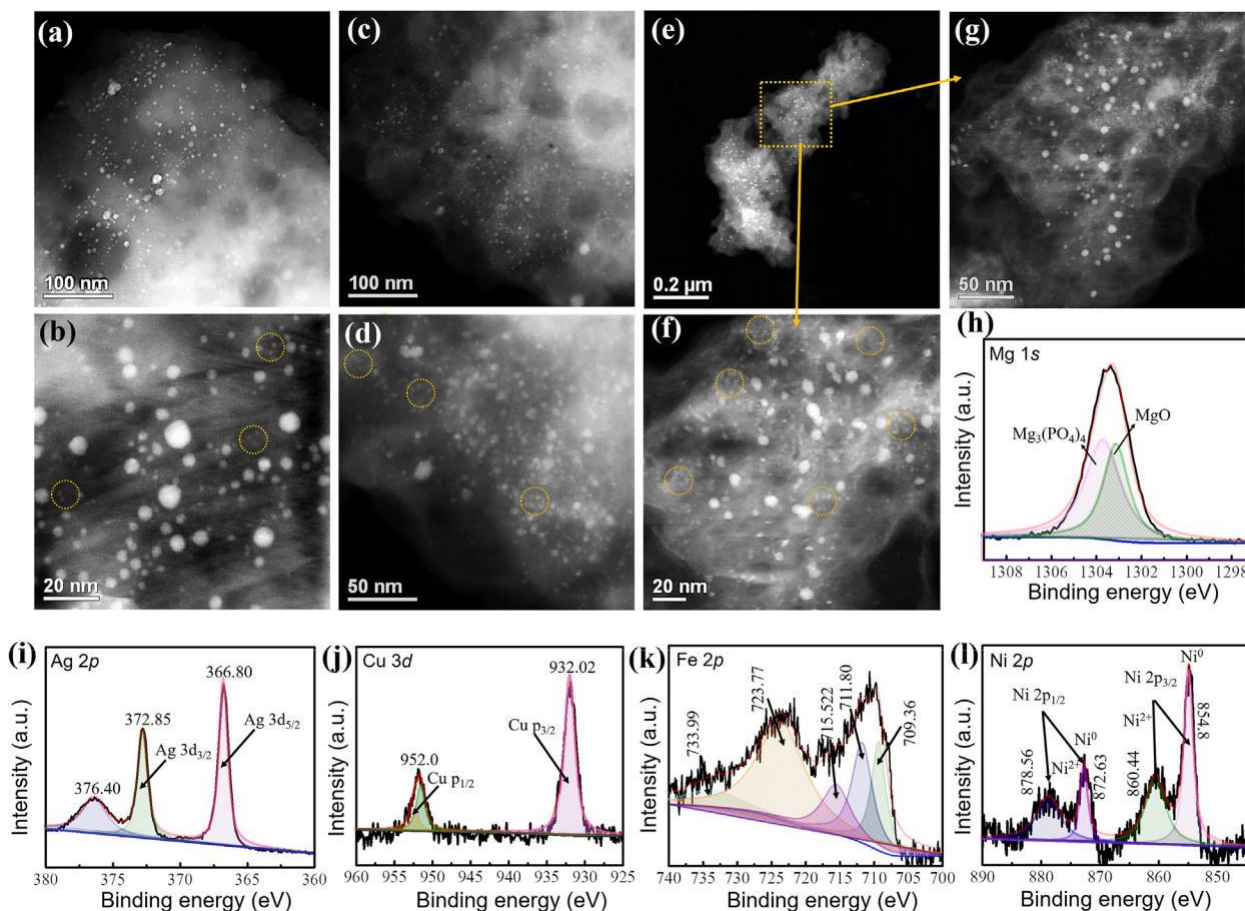


Fig. 3. HAADF-SREM images of the (a and b) CuAgFe/P-MgO catalyst prepared by IP-D with 0 LC solution and three metal precursors, i.e., Cu(NO₃)₂, AgNO₃, and Fe(NO₃)₂, (c and d) CuAgNi/P-MgO catalyst prepared by IP-D with 0 LC solution and three metal precursors, i.e., Cu(NO₃)₂, AgNO₃, Ni(NO₃)₂ and Ni(NO₃)₂, and (e-g) CuAgFeNi/P-MgO catalyst prepared by IP-D with 0 LC solution and three metal precursors, i.e., Cu(NO₃)₂, AgNO₃, Ni(NO₃)₂ and Fe(NO₃)₂. HR-XPS spectra of (h) Mg 1s, (i) Ag 2p, (j) Cu 3d, (k) Fe 2p, and (l) Ni 2p for the CuAgFe/P-MgO catalyst.

8 mg of catalyst and 4 mM of 4NP. Additionally, reduction reactions were conducted in a water bath in darkness with temperatures ranging from 25 LC or 40 LC, yielding 4AP with a conversion of 99.6% and 99.5%, respectively, indicating that CuAgFeNi HEA-NPs are fundamentally active under illuminated and dark conditions.

CuAgFeNi HEA-NP is a well-known photothermal agent compared to carbon-based materials, such as graphite and reduced graphene oxide [28]; therefore, during the reduction reaction under UV light, the spontaneous surface temperature increased to between 30 LC and 35 LC (Fig. 4d and e, simulated light and natural light). However, when the same reduction reaction was conducted in the ambient temperature of the photoreactor, the temperature was controlled at 25 LC, affording a slightly lower yield of 90% for 4NP conversion (Fig. 4d and e, “light with temperature stabilized at 25 LC”). Accordingly, the control of the reduction reactions in the absence of light at 30 LC or 35 LC yielded a lower efficiency (32% and 33%, respectively, Fig. 4d and e “dark”) than the reduction reaction under simulated and natural light, indicating that NPs acted not only via photothermal process but also via intermediate photoexcited types. Correspondingly, the absorption of all simulated light can be understood by combining distinct 3d transition metals, and the optical absorptions can be enhanced by adding Fe and Ni owing to the correlation between the performance and dissimilar 3d band-restricted energy and d-d interband transitions.

3.3. Recyclability of MENPs

The recyclability of the CuAgFeNi catalyst was examined for 20 cycles following reduction reactions using 4 mM 4NP and 8 mg of the catalyst (at its maximum activity, Fig. 4f). Even after 20 cycles, the loss in catalytic performance was marginal (100% conversion and 90% selectivity). Additionally, the XPS results of the reduction reaction (Fig. S11) following the recycling test demonstrated that the catalytic structure retained its characteristics. The Ag 3d high-resolution XPS spectra following the reaction were identical, demonstrating the typical spin-orbit splitting of the Ag atoms, resulting in two different chemical status Ag 3d_{5/2} and Ag 3d_{3/2} peaks separated by 6 eV, confirming AgCuFeNi HEA-NPs and AgCuFeNi-Janus-NPs. The Cu 2p spectra also displayed the characteristic doublet owing to spin-orbit splitting, yielding Cu 2p_{3/2} and Cu 2p_{1/2} peaks separated by 19.9 eV, indicating the existence of Ag-CuFeNi HEA-NPs. The Fe 2p and Ni 2p core level spectra (Fig. S11) revealed a spin-orbit splitting (two primary doublets), Fe/Ni 2p_{3/2} and Fe/Ni, corresponding to the CuAgFeNi nanoalloy on the surface and within the P-MgO support. In addition to high performance, the CuAgFeNi catalyst has considerable reduction potential to decrease a large array of functional group-containing compounds, regardless of the presence of diverse functionalities. Some electron-withdrawing functional groups, such as -I, -Cl, and -CN, on the phenol ring, were sensitive to the reduction reaction of the NO₂ group (Fig. 4g). However, these

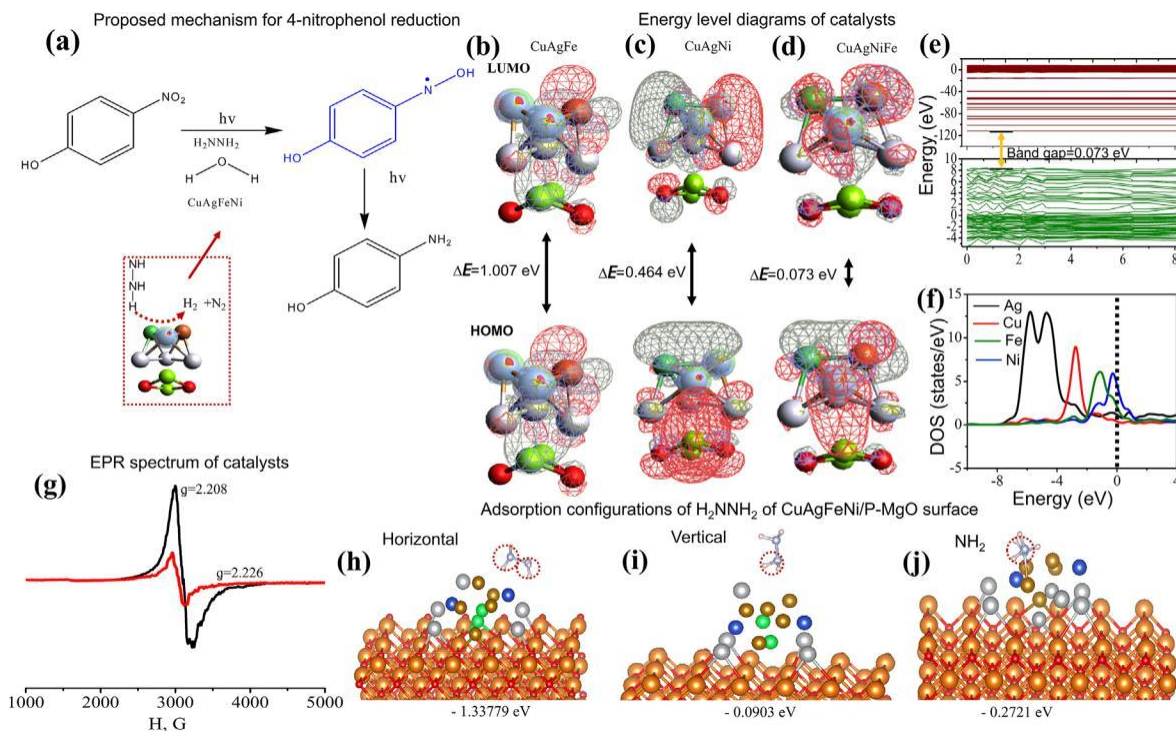


Fig. 5. Proposed mechanism of reduction. (a) The possible reduction mechanism associated with 4-NP of the CuAgNiFe NPs, (b-d) frontier molecular orbitals (HOMO and LUMO) of CuAgFe, CuAgNi, and CuAgNiFe catalyst, respectively, (e) bandgap of CuAgNiFe NPs, (f) total and partial DOS of the metal element in the CuAgNiFe catalyst, (g) the EPR spectrum of CuAgFe and CuAgFeNi/P-MgO catalysts. Adsorption of H_2NNH_2 : (h) horizontal, (i) vertical, and (j) NH_2 on the CuAgNiFe surface.

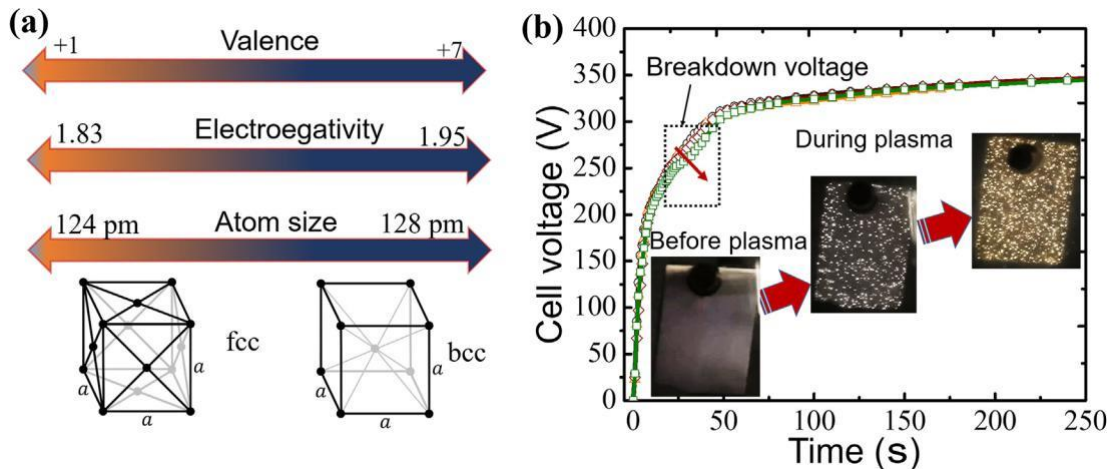


Fig. 6. (a) d-block metals and their various physiochemical properties and (b) the time relations of cell voltage (rms) in the phosphate-based electrolyte during IP-D.

structures, which afford strong immiscibility, quick oxidation, and failure of metallic alloying (Scheme 1). To achieve extreme mixing and overcome immiscibility, the voltage–time (V–t) curves were plotted (Fig. 6b), revealing three steps at 100 A m^{-2} along with an almost linear rise in the voltage with time owing to defective P-MgO on the anode surface growth up to the first bending voltage with the dissolution of the Mg alloy. This suggests a change in the support structure from a passive category to a porous category. After increasing the breakdown voltage to 130 V, a large number of tiny white sparking discharges formed on the anode surface, followed by an increase in the spark size and a drop in the number of sparks. To understand the synthesis of CuAgFeNi HEA-NPs, we used a high local plasma temperature and HEA-based plasma discharge to form small liquid droplets of multielement solutions. The

plasma discharge enabled the formation of homogeneous CuAg-FeNi HEA-NPs by inducing a high local temperature that effectively increased the entropy contribution (TDS_{mix}). From the example of the CuAgNi system, it is evident that increasing the temperature narrows the miscibility gap (Fig. 7a-d). Consequently, the liquid becomes miscible in every composition range over 3000 K. Additionally, mixing entropy increases proportionally to the number of components (Fig. 6e-j). It was also estimated that the CuAgNiFe quaternary system exhibited 2.5 fold higher mixing entropy than that CuAg binary system. At the high temperature caused by plasma discharge, the mixing enthalpy (DH_{mix}) could be exceeded by entropy contribution (Fig. 7i-j), and the system would become completely miscible. Correspondingly, small liquid droplets of HEA would crystallize into single NPs without element

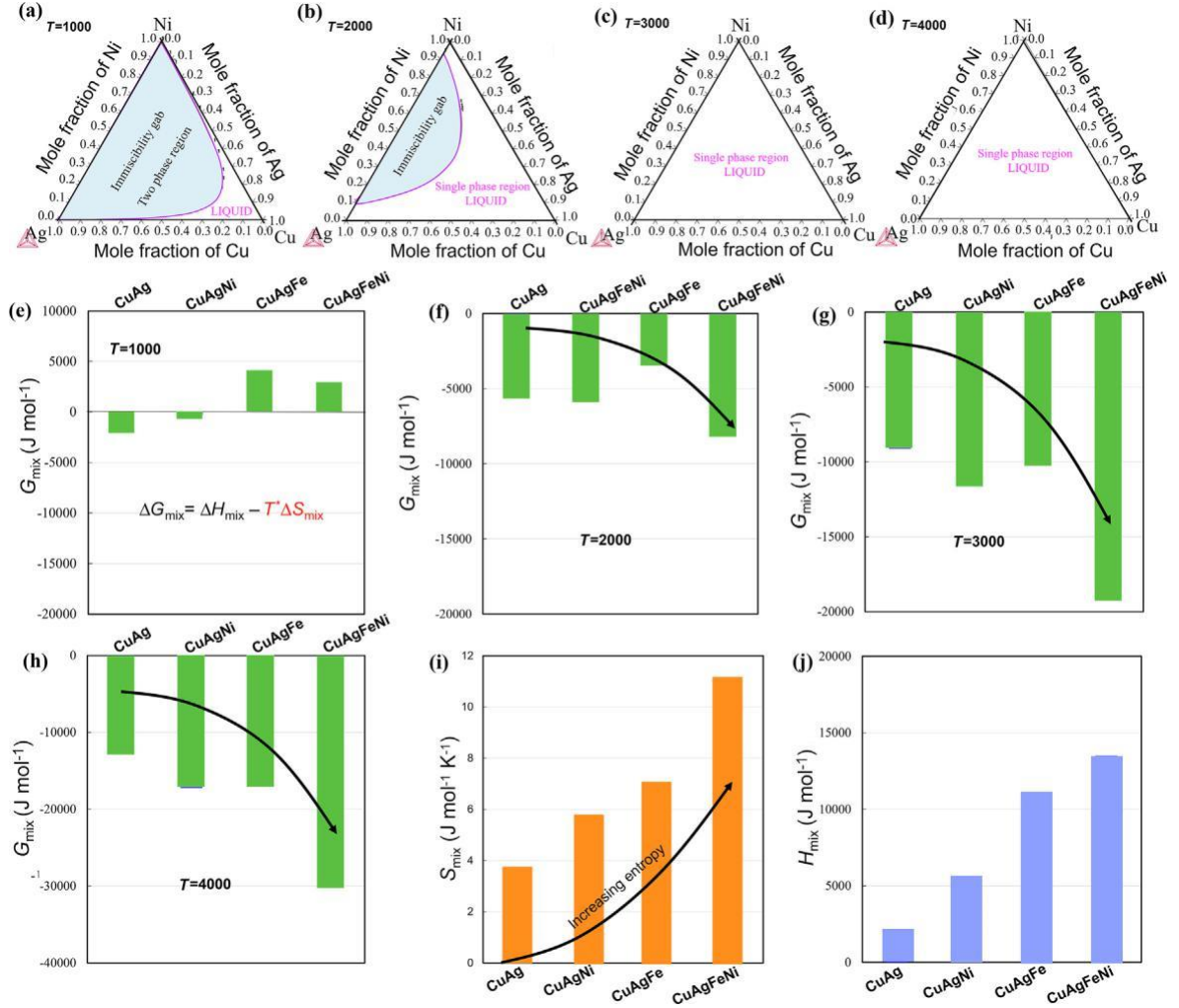


Fig. 7. Isothermal setting of CuAgFeNi phase diagram at (a) 1000 K, (b) 2000 K, (c) 3000 K, and (d) 4000 K. Gibbs free energy diagram of CuAg, CuAgNi, and CuAgFe, and CuAgFeNi at (e) 1000 K, (f) 2000 K, (g) 3000 K, and (h) 4000 K. Estimated mixing of (i) the entropy (DS_{mix}) and (j) mixing enthalpy (DH_{mix}) for CuAg, CuAgNi, CuAgFe, and CuAgFeNi system.

segregation, particle agglomeration/aggregation, or phase separation in the system with a greater number of components. Furthermore, the reported results indicate that some degree of short-range ordering is anticipated in the modeled NPs: Cu, Ag, Fe, and Ni atoms exhibit a strong repulsive magnetic interaction between atom pairs in CuAgFeNi HEA-NPs prepared with a nonequilibrium preparation designated as focused herein. Our atomistic modeling reveals that quenched CuAgFeNi HEA-NPs were kinetically trapped in homogeneous NPs, which are stable at room temperature, via plasma discharge with only little short-range chemical ordering over the examined electrical field range (0.2–0.6 V/Å). Our electrical field effects are consistent with thermodynamic prediction, validating the tendency of various metal compositions to form a single solid-solution phase. In other words, all magnetic moments (short bond and long bond) in magnetically active CuAgFeNi HEA-NPs have significant antiferromagnetic next-nearest-neighbor couplings. Moreover, magnetic moments of CuAgFeNi catalysts are vertical to one another, which can weaken interactions between them. In comparison to conventional synthesis methods [31–34], the impulse plasma deposition method could overcome the immiscibility between different elements by creating liquid metal alloy droplets at high plasma discharge, followed by quick cooling to preserve the alloy mixing to a significant extent. The CuAgFeNi HEA-NPs could aid in the preparation of metal alloys by increasing

entropy ($DG_{mix} = DH_{mix} - TDS_{mix}$), and the increased entropy provides slow diffusion and severe lattice distortion, stabilizing the alloy structures against elemental segregation and nanoscale phase separation, confirming the existence of a solid-solution structure.

In our proposal, kinetic and thermodynamic HEA advantage alloy production was observed to match the following criteria: (i) the mixing enthalpy ($11.6 < DH_{mix} < 3.3$ kJ/mol) and (ii) atomic differences (d 6.5%). Thermodynamically, electrical field and high-local-temperature driven HEA favors a random mixing of alloy structure formation depending on the DG_{mix} but an increase in the DS_{mix} will typically decrease DG_{mix} and thus drive alloy formation. From a kinetic standpoint, a high (TDS_{mix}) structure provides a random mixing of distinct transition elements, affording a considerable lattice strain within MENPs. The distorted chemical structures can furthermore “freeze” or “trap” the mixing of distinct elements inherited from a high-temperature-local-plasma-discharge and electrical field owing to obstacles in structural relaxation and diffusion of atoms. Therefore, the electrical field and entropy-driven approach is an important way for alloy mixtures but the precise evaluation of each contributing parameter will require additional trials and maybe a data-driven discovery method. To understand the changes in the direction and isotropy of metal atoms on a P-MgO substrate in the presence of an external

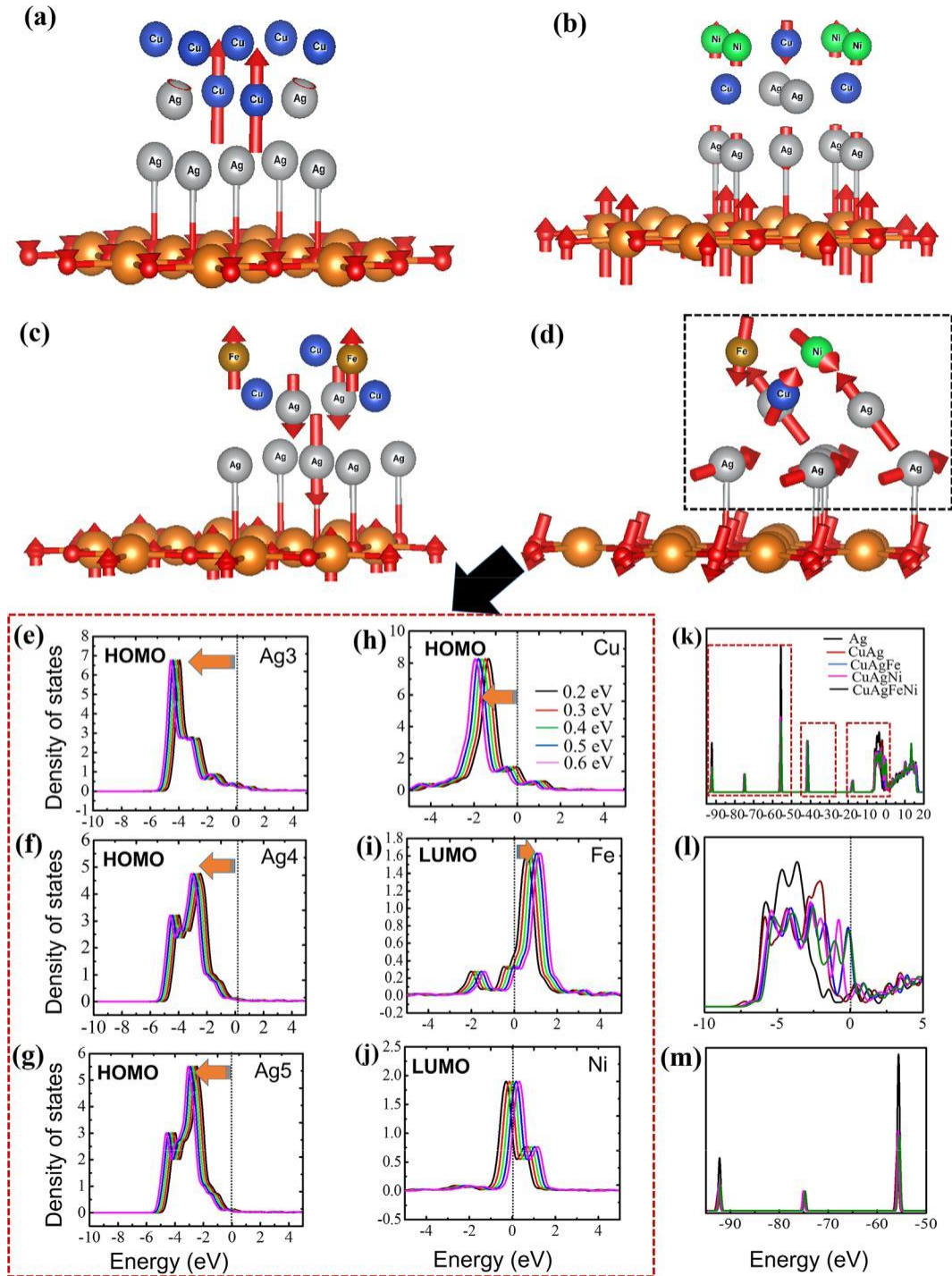


Fig. 8. The magnetic system of the following: (a) CuAg, (b) CuAgNi, (c) CuAgFe, and (d) CuAgFeNi. Total DOS: (e) Ag3, (f) Ag4, (g) Ag5, (h) Cu, (i) Fe, and (j) Ni, (k-m) including the total DOS of Ag, CuAg, CuAgFe, CuAgNi, and CuAgFeNi.

electric field, the effects of the external electric field on the inter-actions between metal atoms under variable electric field (0.2, 0.3, 0.4, 0.5, and 0.6 V/Å) were studied.

To comprehend the change in the electronic properties of CuAg-FeNi HEA-NPs on the P-MgO surface, an external variable electric field (i.e., electron transfer) was introduced into the investigated nanosystem. This generated the paramagnetic moment of deposited atoms on the P-MgO surface; this indicates that when the temperature T was increased in the discharge channel, more atoms were inserted into defects, and the superposition atom structure formed after applying the electric field, the entropy of NPs

increased with decreasing static permittivity (ϵ_s) of the deposited NPs [14,35-37]. Paramagnetic moments of different metal atoms are differently aligned in a paramagnet on a P-MgO support by applying an external electric field and increasing ϵ_s (Fig. 8a-d). Because electron transfer occurs between Fe and the ternary (Ag-Cu-Ni) system from d-d orbitals via agnostic interaction, the internal electric fields are oriented in different directions owing to the insertion of the Fe atom, which has high paramagnetic properties compared to other atoms (Fig. 8d). The calculated DOS diagram of multiple elements demonstrates that the peaks in the range from 4 to 2 eV and the peak observed at 1.86 eV

correspond to the Ag-4d and Cu-3d orbitals, and are located near and above the Fermi level, respectively, indicating that the Ag-4d and Cu-3d orbitals are empty and can accept electrons. Fig. 8(e-m) presents a different perspective of the DOS diagram of Fe-3d, clearly illustrating the accumulation of electrons around the LUMO of Fe, which indicates a donation interaction between Fe and the ternary system (Ag-Cu-Ni) [38-40].

4.1. Benchmarking of the catalyst

CuAgFeNi/P-MgO prepared using the IP-D method maintained its durability and catalytic performance (4-NP yield was 100%). Based on the analysis shown in Table S2 and Fig. S4, the present CuAgFeNi/P-MgO catalytic discovered its high reduction performance and transformative activity based on TOF [41-48].

5. Conclusions

The IP-D method provides an excellent platform to synthesize small-sized CuAgFeNi HEA-NPs using a straightforward method at atmospheric pressure. Immiscible MEs are alloyed into single NPs on P-MgO with the following features: (i) nonequilibrium processing, where plasma discharges take milliseconds and are energy efficient generating HEA-NPs via rapid cooling of the melt during IP-D process, thus avoiding phase separation among immiscible metal elements by increasing the local electron temperature via an electrical field, and (ii) maximization of entropy contribution to miscibility using multicomponents and a high local temperature. This strategy also exhibits universality, potential scalability, and tunability; the local plasma electron temperature in the plasma channel is higher than the chemical decomposition caused by the heating of any metal salt, which promotes the homogeneous mixing of any combination of metal elements. CuAgFeNi/P-MgO exhibits superior catalytic activity, recyclability, and stability in the reduction of nitro to amino groups compared to those of other leading photo and thermal catalysts. Catalyst surface modification with new metals and nonmetals to tailor the surface energy and match the frontier orbitals of other substrates, such as Ti, Al, and Mg, could further enhance the standing and utility of the present findings.

Declaration of competing interest

The authors declare that they have no known competing financial interests or personal relationships that could have appeared to influence the work reported in this paper.

Acknowledgements

This research was supported by the National Research Foundation (NRF) of South Korea (2022R1A2C1004392).

References

- [1] Z. Xu, X. Zhang, X. Xingdong, J. Fang, Z. Yufeng, X. Liu, W. Zhu, Y. Yan, Z. Zhuang, *ACS Nano* 15 (2021) 7131–7138.
- [2] G. Chen, Y. Zhao, G. Fu, P.N. Duchesne, L. Gu, Y. Zheng, X. Weng, M. Chen, P. Zhang, C.-W. Pao, J.F. Lee, N. Science 344 (2014) 495–499.
- [3] M. Cu, C. Yang, S. Hwang, M. Yang, S. Overa, Q. Dong, Y. Yao, A.-H. Brozena, D.-A. Cullen, M. Chi, T.-F. Blum, D. Morris, Z. Finck, X. Wang, P. Zhang, V.-G. Goncharov, X. Guo, J. Luo, Y. Mo, F. Jiao, L. Hu, *Sci. Adv.* 8 (2022) eabm4322.

- [4] H. Wang, S. Xu, C. Tsai, Y.-Li, C. Liu, J. Zhao, Y. Liu, H. Yuan, F. Abild-Pedersen, F.-B. Prinz, J.-K. Nørskov, Y. Cui, *Science*, 354 (2016) 1031–1036.
- [5] D.B. Miracle, O.N. Senkov, *Acta Materialia*, 122 (2017) 448–511.
- [6] J. Zhang, H. Wang, L. Wang, S. Ali, C. Wang, L. Wang, X. Meng, B. Li, D.-S. Su, F.-S. Xiao, *J. Am. Chem. Soc.* 141 (2019) 2975–2983.
- [7] Y. Yao, Z. Huang, T. Lia, H. Wang, Y. Liud, H.-S. Steine, Y. Mao, J. Gao, M. Jiao, Q. Dong, J. Dai, P. Xied, H. Xie, S.-D. Lacey, I. Takeuchi, J.-M. Gregoire, R. Jiang, C. Wange, A.-D. Taylor, S.-Y. Reza, L.-Hu, *PNAS*, 117 (2020) 6316–6322.
- [8] P.-C. Chen, X. Liu, J.-L. Hedrick, Z. Xie, S. Wang, Q.-Y. Lin, M.-C. Hersam, V.-P. Dravid, C.-A. Mirkin, *Science* 352 (2016) 1565–1569.
- [9] H. Li, Y. Han, H. Zhao, W. Qi, D. Zhang, Y. Yu, W. Cai, S. Li, J. Lai, B. Huang, L. Wang, *Nat. Commun* 11 (2020) 5437.
- [10] Y. Yao, Z. Huang, P. Xie, S.-D. Lacey, R.-J. Jacob, H. Xie, F. Chen, A. Nie, T. Pu, M. Rehwaldt, D. Yu, M.-R. Zachariah, C. Wang, R.-S. Yassar, J. Li, L. Hu, *Science* 359 (2018) 1489–1494.
- [11] H. Qiao, M.-T. Saray, X. Wang, S. Xu, G. Chen, Z. Huang, C. Chen, G. Zhong, Q. Dong, M. Hong, H. Xie, R. Shahbazian-Yassar, L. Hu, *ACS Nano* 15 (2021) 14928–14937.
- [12] S. Gao, S. Hao, Z. Huang, Y. Yuan, S. Han, L. Lei, X. Zhang, R. Shahbazian-Yassar, J. Lu, *Nature Communications*, 11 (2020) 2016.
- [13] M. Bondesgaard, N.-L.-N. Broge, A. Mamakhel, M. Bremholm, B.-B. Adv. *Funct. Mater.* 29 (2019) 1905933.
- [14] W. Al Zoubi, N. Nashrah, R.A.K. Putri, A.W. Allaf, B. Assfour, Y.G. Ko, *Mater. Today Nano* 18 (2022) 100213.
- [15] D. Wu, K. Kusada, T. Yamamoto, T. Toriyama, S. Matsumura, S. Kawaguchi, Y. Kubota, H. J. Am. Chem. Soc., 142 (2020) 13833–13838.
- [16] N. L. N. Broge, M. Bondesgaard, F. Søndergaard-Pedersen, M. Roelsgaard, B. B. *Angew. Chem. Int. Ed.* 59 (2020) 21920–21924.
- [17] X. Chen, C. Si, Y. Gao, J. Ftenzel, J. Sun, G. Eggeler, Z. Zhang, J. Power, *Sources* 273 (2015) 324.
- [18] Y. Yao, Z. Huang, P. Xie, S.D. Lacey, R.-J. Jacob, H. Xie, F. Chen, A. Nie, T. Pu, M. Rehwaldt, D. Yu, M.-R. Zachariah, C. Wang, R. Shahbazian-Yassar, J. Li, L. Hu, *Science* 359 (2018) 1489–1494.
- [19] X. Yu, C. Hu, P. Ji, Y. Ren, H. Zhao, G. Liu, R. Xu, X. Zhu, Z. Li, Y. Ma, L. Ma, *Appl. Catal. B* 310 (2022).
- [20] Z. Li, K.G. Pradeep, Y. Deng, D. Raabe, C.C. Tasa, *Nature* 534 (2014) 227–230.
- [21] X. Wang, X. Li, H. Fan, M. Miao, Y. Zhang, W. Guo, Y. Fu, *J. Energy. Chem.* 67 (2022) 276–289.
- [22] X. Liang, J. Chen, B. Hong, T. Wan, W. Weng, W. Xiao, *J. Energy. Chem.* 74 (2022) 212–217.
- [23] Y. Pan, M. Wang, M. Li, G. Sun, Y. Chen, Y. Liu, W. Zhu, B. Wang, *J. Energy. Chem.* 68 (2022) 699–708.
- [24] H. Jiang, X. Liu, D. Wang, Z. Qiao, D. Wang, F. Huang, H. Peng, C. Hu, *J. Energy Chem.* doi.org/10.1016/j.jechem.2023.01.009.
- [25] Y. Qiao, Y. Ni, Z. Chen, F. Kong, R. Li, C. Zhang, A. Kong, Y. Shan, *J. Electrochem. Soc.* 166 (2019) H272–H282.
- [26] F. Xie, M.-T. Zhang, *J. Energy. Chem.* 63 (2021) 1–7.
- [27] Y. Liao, Y. Li, R. Zhao, J. Zhang, L. Zhao, L. Ji, Z. Zhang, X. Liu, G. Qin, X. Zhang, *National Science Review* 9 (2022) 041.
- [28] A. Rodríguez-Gómez, E. Lepre, L. Sánchez-Silva, N. López-Salas, A. Raquel de la Osa, *J. Energy Chem.* 66 (2022) 168–180.
- [29] C. Chu, S. Rao, Z. Ma, H. Han, *Appl. Catal. B* 256 (2019).
- [30] S. Zhang, C.R. Chang, Z.Q. Huang, J. Li, Z. Wu, Y. Ma, Z. Zhang, Y. Wang, Y. Qu, *J. Am. Chem. Soc.* 138 (2016) 2629–2637.
- [31] J. He, N. Li, Z.-G. Li, M. Zhong, Z.-X. Fu, M. Lu, J.-C. Yin, Z. Shen, W. Li, J. Zhang, Z. Adv. *Funct. Mater* 31 (2021) 2103597.
- [32] I.A. Abdel-Latif, H.Y. Ammar, *Results Phys* 7 (2017) 4419–4426.
- [33] C. Yang, B.-H. Ko, S. Hwang, Z. Liu, Y. Yao, W. Luc, M. Cui, A.S. Malkani, T. Li, X. Wang, J. Dai, B. Xu, G. Wang, D. Su, F. Jiao, L. Hu, *Sci. Adv.* 6 (2020) eaz6844.
- [34] W. Al Zoubi, M.P. Kamil, S. Fatimah, N. Nashrah, Y.-G. Ko, *Prog. Mater. Sci.* 112 (2020) 100663.
- [35] G.P. Johari, *J. Chem. Phys.* 138 (2013).
- [36] D.-V. Talapin, E.-V. Shevchenko, C.-B. Murray, A.-V. Titov, P. Kral, *Nano Letters*, 7 (2007) 1213–1219.
- [37] W. Al Zoubi, A.-W. Allaf, B. Assfour, Y.-G. Ko, *ACS App. Mater. Interfaces*, 14 (2022) 6740–6753.
- [38] C. Zhang, C. Jiang, Q. Tang, Z. Meng, Y. Li, Y. Wang, Y. Cui, W. Shi, S. Yu, H. Tian, W. Zhen, *J. Energy Chem.* 78 (2023) 438–446.
- [39] J. Huang, W. Zhou, X. Luo, Y. Ding, D. Peng, M. Chen, H. Zhou, C. Hu, C. Yuan, S. Wang, *Chem. Eng. J.* 454 (2023).
- [40] J. Yang, H.-Q. Chen, N. Shi, T. Wang, J. Liu, W.-P. Pan, *Chem. Eng. J.* 428 (2022).
- [41] X. Huang, G. Yang, S. Li, H. Wang, Y. Cao, F. Peng, H. Yu, *J. Energy Chem.* 68 (2022) 721–751.
- [42] S. Zhang, W. Huang, X. Fu, X. Zheng, S. Meng, X. Ye, S. Chen, *Appl. Catal. B* 233 (2018) 1–10.
- [43] S. Zhang, W. Huang, X. Fu, G. Chen, S. Meng, S. Chen, *J. Hazard. Mater* 360 (2018) 182–192.
- [44] A. Kumar, B. Paul, R. Boukherroub, *J. Hazard. Mater* 387 (2020).
- [45] X. Lyu, W. Zhang, S. Liu, X. Wang, G. Li, B. Shi, K. Wang, X. Wang, Q. Wang, Y. Jia, *J. Energy Chem.* 53 (2021) 192–196.
- [46] A. Goswami, R.G. Kadam, J. Tucek, D. Bousa, R.S. Varma, M. Gawande, R. Zboril, *Chem. Eng. J.* 382 (2020).
- [47] W. Gong, Y. Lin, C. Chen, M. Al-Mamun, H.S. Lu, G. Wang, H. Zhang, H. Zhao, *Adv. Mater* 31 (2019) 1808341.
- [48] L. Lin, R. Gao, X. Liang, Q. Yu, Y. Deng, J. Liu, M. Peng, Z. Jiang, S. Li, Y.W. Li, X.D. Wen, W. Zhou, D. Ma, *Nat. Nanotechnol* 14 (2019) 354–361.